

Journal of Sensors

A Novel Downward-Looking Linear Array SAR Imaging Method Based on Multiple Measurement Vectors Model with $L_{2,1}$ -Norm

Tianchi Sun,^{1,2} Le Kang,^{1,2} Jia-cheng Ni,^{1,2} Qun Zhang^{1,2,3} and Ying Luo^{1,2}

¹ Information and Navigation College, Air Force Engineering University, 710077, China.

² Collaborative Innovation Center of Information Sensing and Understanding, 710077, China.

³ Key Laboratory for Information Science of Electromagnetic Waves (Ministry of Education), Fudan University, 200433, China.

Correspondence should be addressed to Jia-cheng Ni, E-mail: littlenjc@sina.com

Abstract

Downward-Looking Linear Array Synthetic Aperture Radar (DLLA SAR) is a kind of three-dimensional (3-D) radar imaging system. To obtain the super-resolution along the cross-track direction of DLLA SAR, the sparse regularization models with Single Measurement Vector (SMV) have been widely applied. However, the robustness of the sparse regularization models with SMV is unsatisfactory, especially in the low Signal-to-Noise Rate (SNR) environment. To solve this problem, we proposed a novel imaging method for DLLA SAR based on the Multiple Measurement Vectors (MMV) model with $L_{2,1}$ -Norm. At first, we exchange the processing order between the along-track (AT) and the cross-track (CT) to keep the same sparse structure of the signal in the cross-track domain so that we can establish the imaging problem as a sparse regularization model based on the MMV model. Moreover, the mixed $L_{2,1}$ -norm is introduced into the regularization term of the MMV model. Finally, the modified Orthogonal Matching Pursuit (OMP) algorithm is designed for the MMV model with $L_{2,1}$ -Norm. The simulations verify that the proposed method can obtain the cross-track super-resolution in the lower SNR environment and require lower computation compared with the conventional methods.

Introduction

Synthetic aperture radar (SAR) has been widely applied in the remote sensing area to obtain radar images without being affected by weather, daylight, or cloud coverage [1,2]. Over past decades, three-dimensional (3-D) SAR, which can be roughly divided into three types including Circular SAR (CSAR) [3], Tomographic SAR (TomoSAR) [4], and array SAR [5], has attracted wide attention as a development trend of SAR. Downward-looking linear array (DLLA) 3-D SAR is a kind of array SAR [6]. Due to the downward-looking imaging geometry and the linear array antennas distributed along the wing of the rectilinearly moving platform, the DLLA 3-D SAR can generate 3-D radar images of the directly overflowed scene [7,8]. While combining the 2-D SAR imaging algorithms, several imaging algorithms of DLLA 3D SAR are proposed, e.g., 3-D range-Doppler (3DRD) algorithm [9], 3-D chirp scaling algorithm [10], and 3-D polar format algorithm [11]. For these imaging algorithms, the resolutions in range, along-track (AT) and cross-track (CT) directions are obtained by pulse compression, synthetic aperture, and beam-forming, respectively. However, the CT

resolution of DLLA 3-D SAR is mainly determined by the length of the linear array along the CT direction, which leads to poor resolution in the CT direction since the length of the linear array is limited by the platform.

Except for improving the CT resolution by a longer linear array, many super-resolution methods are introduced to DLLA 3-D SAR imaging, e.g., compressed sensing (CS) [12]. In the CS theory, the sparse signals can be exactly recovered with a high probability from the low-dimensional measurement signal [13]. Since the signal of DLLA 3-D SAR is sparse in the CT domain, CS is used in the CT domain of DLLA 3-D SAR [14-22]. In [14], the signal processing in the CT domain is transformed into the sparse reconstruction with L_0 regularization from noisy measurements. To realize the CT super-resolution with a nonuniform linear array, the Truncated SVD-based CS method is proposed [15]. In [16], a DL sparse LA (DLSLA) 3-D SAR image reconstruction algorithm that combines polar formatting and L_1 regularization is presented, which can be employed to airborne DLLA 3-D SAR with nonuniform and sparse cross-track virtual phase centers. Considering the basis mismatch problem, the methods based on atomic norm [17-20] transform the cross-track processing into a semidefinite programming problem. However, the CT compression of the above methods is realized by the Single Measurement Vector (SMV) model. Although these SMV-based methods can achieve better resolution and lower sidelobes in the CT domain, the robustness of the sparse regularization models with the SMV model is unsatisfactory, especially in the low Signal-to-Noise Rate (SNR) environment [13]. Compared with the classical Single Measurement Vector (SMV) model, the Multiple Measurement Vectors (MMV) model of CS theory can enhance the computational efficiency and elevate the anti-noise performance by utilizing the same sparse structures of multiple measurement signals [21]. The MMV model has been successfully introduced into 2-D SAR imaging since the sparse structures of different pulses are the same in SAR measurements [22, 23]. The different pulses in SAR are equal to the different AT sampling points in DLLA SAR, so the MMV model has been directly utilized in the AT domain [24]. However, the CT sparse structures of different pulses are different so that the MMV model cannot be directly utilized in the CT domain.

In this paper, a novel imaging method for DLLA 3D SAR based on the MMV model and a mixed matrix norm is proposed. At first, we construct the same CT sparse structure of different pulses by exchanging the processing sequence of CT and AT domain so that the imaging problem can be regarded as a sparse regularization model based on the MMV model. Moreover, the mixed $L_{2,1}$ -norm is introduced into the regularization term of the MMV model. Finally, the proposed imaging model is solved by the modified MMV Orthogonal Matching Pursuit (MMV-OMP) algorithm. The proposed method can obtain the CT super-resolution in the lower SNR environment and require lower computation compared with the conventional methods, which is verified by simulation experiments.

Reviews of SMV Model and MMV Model

In CS theory, the signal $s \in \mathbb{C}^Q$ is sparse if the sparse level K , the number of the non-zero values in s , is much less than Q . For a down-sampling matrix $\Phi \in \mathbb{C}^{N \times Q}$, $N < Q$, the low-dimensional measurement vector of s can be written as $y = \Phi s$, $y \in \mathbb{C}^{N \times 1}$. The sparse representation of s can be written as $s = \Psi x$, where x is sparse and Ψ is the sparse basis matrix. (When s is sparse, the sparse basis matrix Ψ is the unit matrix). If the measurement matrix $A = \Phi \Psi$ satisfies the Restricted Incoherence Property (RIP), the problem, which is to

85 solve the sparse signal \mathbf{x} on the condition that the \mathbf{y} and \mathbf{A} are known, can be transformed
 86 as the 1-norm minimization [12]:

$$87 \quad \min \|\mathbf{x}\|_1, \quad \text{s.t.} \quad \mathbf{y} - \mathbf{A}\mathbf{x} < \varepsilon \quad (1)$$

88 where $\|\cdot\|_1$ is the 1-norm operator and ε is a value related to the noise.

89 When the signal \mathbf{y} is a vector, \mathbf{y} is called the single measurement signal, and the model in
 90 Equation 1 is called the SMV model. The SMV model can be solved by many CS
 91 reconstruction algorithms. Here we briefly introduce the OMP algorithm [25] in Table. 1,
 92 where T is the matrix transposition, $^{(k)}$ is the k th iteration, $\|\cdot\|_1$ is the l_1 norm, the support set
 93 Ω is the index set of non-zero values, \mathbf{A}_Ω is formed by the columns of \mathbf{A} with the index in
 94 Ω .

95 Table 1: SMV-OMP algorithm

Input: vector \mathbf{y} , matrix \mathbf{A} , threshold ε ;
Initialization: residue error vector $\mathbf{r}^{(0)} = \mathbf{y}$; support set $\Omega^{(0)} = \emptyset$;
sparse vector $\mathbf{x}^{(0)} = \mathbf{0}$, iterative number $k=1$;
While $\ \mathbf{r}^{(k-1)}\ _1 > \varepsilon$
Step 1: Find the new support: $\eta_k = \arg \max_{i=1,2,\dots,Q} \ \mathbf{A}_i^T \mathbf{r}^{(k-1)}\ _1$;
Step 2: Update the support set: $\Omega^{(k)} = \Omega^{(k-1)} \cup \{\eta_k\}$;
Step 3: Update the sparse vector $\mathbf{x}^{(k)} = (\mathbf{A}_{\Omega^{(0)}}^H \mathbf{A}_{\Omega^{(0)}})^{-1} \mathbf{A}_{\Omega^{(0)}}^H \mathbf{r}^{(k-1)}$;
Step 4: Update the residue error $\mathbf{r}^{(k)} = \mathbf{y} - \mathbf{A}_{\Omega^{(0)}} \mathbf{x}^{(k)}$, $k = k + 1$;
Output: sparse vector $\mathbf{x}^{(k)}$

96 For L single measurement signals $\mathbf{y}_1, \mathbf{y}_2, \dots, \mathbf{y}_L$ with the same measurement matrix \mathbf{A} , the
 97 SMV model in Equation 1 has to be solved L times to obtain the corresponding sparse signals
 98 $\mathbf{x}_1, \mathbf{x}_2, \dots, \mathbf{x}_L$. However, if the sparse structures of $\mathbf{x}_1, \mathbf{x}_2, \dots, \mathbf{x}_L$ are the same, which means that
 99 the positions of the nonzero values in $\mathbf{x}_1, \mathbf{x}_2, \dots, \mathbf{x}_L$ are the same, the MMV model can be
 100 expressed as [21]

$$101 \quad \min \|\mathbf{X}\|_1, \quad \text{s.t.} \quad \mathbf{Y} - \mathbf{A}\mathbf{X} < \varepsilon \quad (2)$$

102 where $\mathbf{Y} = [\mathbf{y}_1, \mathbf{y}_2, \dots, \mathbf{y}_L]$ and $\mathbf{X} = [\mathbf{x}_1, \mathbf{x}_2, \dots, \mathbf{x}_L]$. In the MMV model, \mathbf{X} can be obtained by
 103 solving Equation 2 only once, so that the MMV model has lower complexity and better anti-
 104 noise performance compared with the SMV model.

105 SMV-based DLLA SAR Imaging Procedure

106 The geometry of DLLA 3D SAR is shown in Figure 1. The radar platform flies along the
 107 flight path of the platform (X -axis), with velocity v at height H . The linear array contains N
 108 antenna elements equally spaced with the distance d , which is mounted underneath the wings

along CT direction (Y -axis). The length of the linear array is $L_y = (N-1)d$. At slow time t_m , the coordinate of the n -th antenna element is (x_m, y_n, H) , where $x_m = vt_m$ and $y_n = -(N-1)d/2 + (n-1)d$. The origin of the coordinate O is the center of the imaging scene.

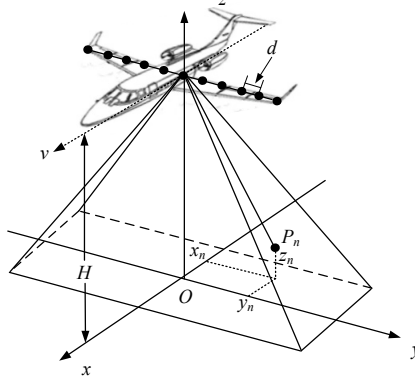


Figure 1: Geometry of DLLA 3-D SAR. The radar platform flies along the X -axis with velocity v at height H . The linear array contains N antenna elements equally spaced with the distance d , which is mounted underneath the wings along the Y -axis.

The antenna element transmits a linear frequency modulation signal in turn and receives the incoming echo signal from the reflection by the scatterers. The echo signal received from the n -th antenna can be written as

$$S(t, t_m, y_n) = \sum_K \sigma_k \text{rect}\left(\frac{t - 2R(t_m, y_n)/c}{T_r}\right) \exp\left(j\pi K_r \left(t - \frac{2R(t_m, y_n)}{c}\right)^2 - j\frac{4\pi}{\lambda} R(t_m, y_n)\right), \quad (3)$$

where t is the fast time, $\text{rect}(\cdot)$ is the unit rectangular function, K is the number of scattering points in the imaging scene, σ_k is the scattering coefficient of the k -th scattering point, c is the light speed, K_r is the chirp rate and λ is the wavelength, T_r is the pulse width, e is the noise, and $R(t_m, y_n)$ is the instantaneous distance between the n -th antenna element and the point scatterer $P_k(x_k, y_k, z_k)$ at the slow time t_m , which can be expressed as

$$R(t_m, y_n) = \sqrt{(vt_m - x_k)^2 + (y_n - y_k)^2 + (H - z_k)^2} \approx R_0 + \frac{(vt_m - x_k)^2}{2R_0} + \frac{y_n^2 - 2y_n y_k}{2R_0}, \quad (4)$$

where $R_0 = (x_k^2 + y_k^2 + (H - z_k)^2)^{1/2}$ is the projected instantaneous distance on the zero-Doppler plane.

The imaging procedure of SMV-based DLLA SAR is shown in Figure 2, which can be divided into range compression, AT compression, and CT compression. At first, the echo signal of Equation 3 is discretized into a 3-D matrix, where N_r , M , and N are the sampling numbers in the range (fast time) domain, AT (slow time) domain and CT domain, respectively.

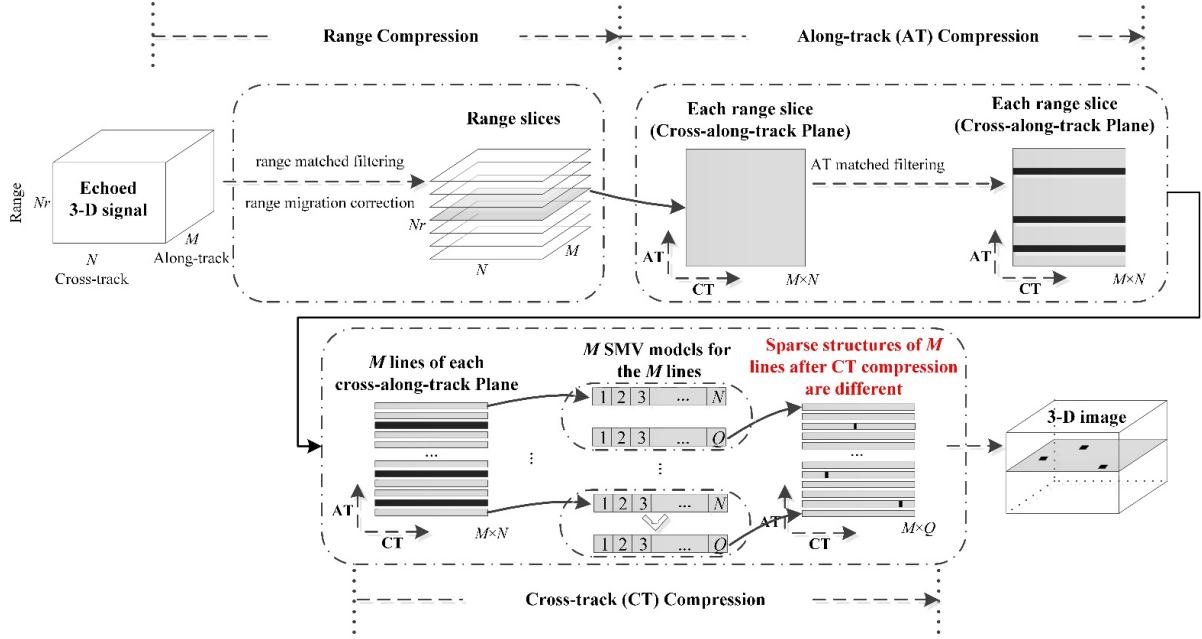


Figure 2: Imaging procedure of SMV-based DLLA 3-D SAR. The imaging procedure can be divided into range compression, AT compression, and CT compression.

The range compression is realized by range matched filtering and range migration correction. After the range compression, the 3-D signal has been focused in the range domain and can be regarded as N_r range slices. Then, the AT compression is realized by the AT matched filtering for each range slice of the 3-D signal. After the AT compression, the signal of each range slice has been focused on the AT domain. In the cross-along-track plane, each line represents the signal vector with the same positions along the range and AT directions. The black lines of the cross-along-track plane mean that the scattering points exist in the corresponding positions along the range and AT directions.

For each line in the cross-along-track plane, the length of the original vector is the CT sampling number N . To obtain the super-resolution along the CT direction, the imaging scene is discretized by Q ($Q > N$) grids along the CT directions. The signal processing of each line in the cross-along-track plane is transformed into an SMV model, in which the original signal of each line is regarded as the measurement signal y and each line after the CT compression is regarded as the sparse signal x . After the CT compression, the sparse structures of the lines in the cross-along-track plane are different because they are determined by the positions of the scattering points. As a result, the condition of the MMV model is not satisfied so that the M lines in each range slice have to be solved by the SMV model independently.

Proposed DLLA SAR Imaging method

In DLLA SAR imaging, there are large amounts of nontarget zones in the different elevations of the 3D scene so that only a few scatterers are presented in the same range cell. As a result, the prerequisite for CS, the sparsity of signal, is satisfied for DLLA SAR imaging. To introduce the MMV model into the CT domain of DLLA SAR, we exchange the processing sequence of the CT compression and the AT compression to construct the same sparse structure after the CT compression.

Range Compression

The proposed imaging procedure of MMV-based DLLA SAR is shown in Figure 3, which can be divided into three steps including range compression, CT compression, and AT compression.

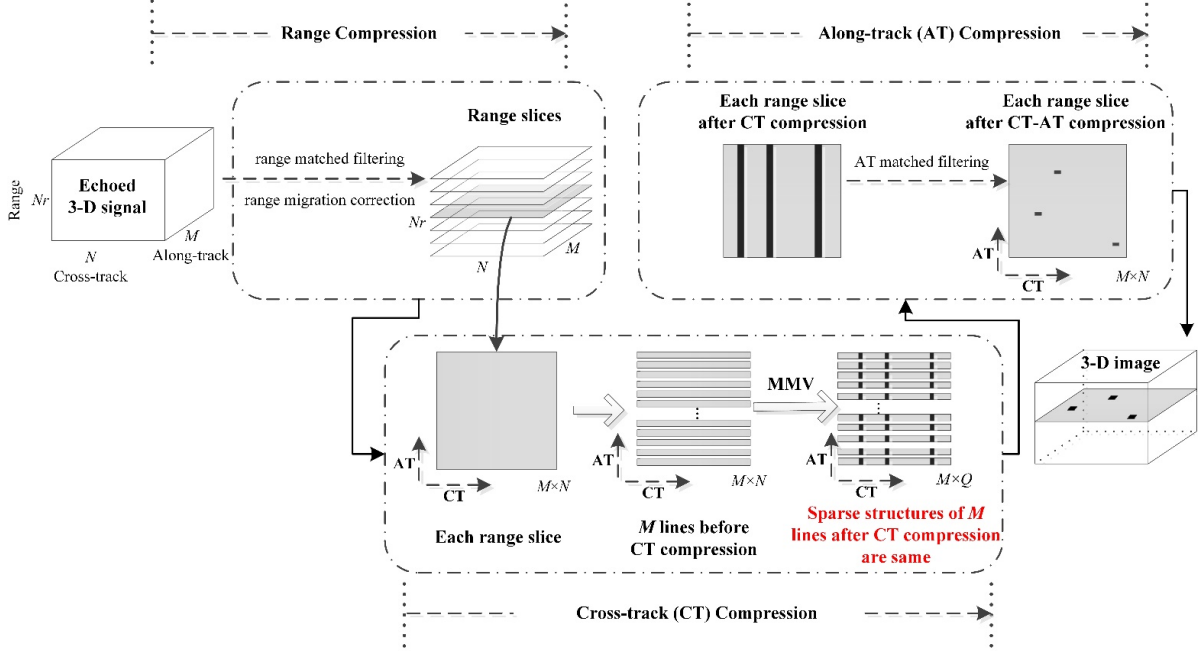


Figure 3: Imaging procedure of MMV-based DLLA 3-D SAR. The imaging procedure can be divided into three steps including range compression, CT compression, and AT compression.

The range compression can be expressed as

$$\begin{aligned}
 S_r(t, t_m, y_n) &= IFT_r \left[FT_r \left[S(t, t_m, y_n) \right] \cdot H_r \cdot H_{rma} \cdot H_{rmc} \right] \\
 &= \sum_K \sigma_k \operatorname{sinc} \left(T_r K_r \left(t - \frac{2R_0}{c} \right) \right) \exp \left(-j \frac{4\pi}{\lambda} R(t_m, y_n) \right) + e \\
 &= \sum_K \sigma_k \operatorname{sinc} \left(T_r K_r \left(t - \frac{2R_0}{c} \right) \right) \exp \left(-j \frac{4\pi}{\lambda} R_0 \right) \exp \left(-j \frac{2\pi (vt_m - x_k)^2}{\lambda R_0} \right) \exp \left(-j \frac{2\pi (y_n^2 - 2y_n y_k)}{\lambda R_0} \right)
 \end{aligned} \tag{5}$$

where FT_r and IFT_r denote the Fourier transformation and inverse Fourier transformation of the range direction, $H_r(f_r) = \operatorname{rect}(f_r/T_r K_r) \exp(j\pi f_r^2/K_r)$ is the range matched filter function, H_{rma} and H_{rmc} denote the range migration correction function in the AT and CT direction, respectively [20]. Since y_n and R_0 are known when the position of the antenna elements and the imaging scene are fixed, the quadratic phase term and the constant phase term in Equation 5 can be compensated and the signal can be expressed as

$$S_r(t, t_m, y_n) = \sum_K \sigma_k \operatorname{sinc} \left(B_r \left(t - \frac{2R_0}{c} \right) \right) \exp \left(-j \frac{2\pi (vt_m - x_k)^2}{\lambda R_0} \right) \exp \left(-j \frac{4\pi y_n y_k}{\lambda R_0} \right) \tag{6}$$

178 where $B_r = T_r K_r$ is the range bandwidth.

179 **Cross-track Compression by the MMV model with $L_{2,1}$ norm**

180 After range compression, each measurement vector is a line along the CT direction so that
 181 each range slice contains M measurement vectors. Since the CT compression is before the AT
 182 compression, the signal of range slice focuses in several lines along the AT direction, which
 183 means that the M measurement vectors after CT compression have the same sparse structure.
 184 As a result, the MMV model can be introduced into the CT compression.

185 The imaging scene is discretized as equal grids $\hat{\mathbf{y}} = [\hat{y}_1; \dots; \hat{y}_N]^T \in \mathbb{C}^{N \times 1}$ along the CT
 186 direction. After cross-track compression, the signal is sparse in cross-track. Thus, we can
 187 recover the cross-track signal from a low-dimensional measurement signal by the CS method.
 188 The measurement signal of the m th pulse with N sample number in cross-track direction can
 189 be expressed as $\mathbf{s}_m = [s(t_m, y_1); \dots; s(t_m, y_N)]^T \in \mathbb{C}^{N \times 1}$. Suppose the corresponding focused
 190 signal after cross-track compression is $\mathbf{g}_m = [g_1(t_m); \dots; g_N(t_m)]^T \in \mathbb{C}^{N \times 1}$. Therefore, the echo
 191 signal of all CT sampling points at slow-time t_m can be written as

$$192 \quad \mathbf{s}_m = [\varphi_1, \varphi_2, \dots, \varphi_N] [g_1(t_m), g_2(t_m), \dots, g_N(t_m)]^T = \mathbf{\Psi} \mathbf{g}_m, m = 1, 2, \dots, M, \quad (7)$$

193 where $\mathbf{\Psi} = [\varphi_1, \varphi_2, \dots, \varphi_N]$ is the sparse basis matrix. The n th column of the sparse basis
 194 matrix $\mathbf{\Psi}$ can be expressed as

$$195 \quad \varphi_n = \left[\exp\left(-j \frac{4\pi}{\lambda R_0} y_1 \hat{y}_n\right), \exp\left(-j \frac{4\pi}{\lambda R_0} y_2 \hat{y}_n\right), \dots, \exp\left(-j \frac{4\pi}{\lambda R_0} y_N \hat{y}_n\right) \right]^T. \quad (9)$$

196 Next, we can get the low-dimensional measurement vector through down-sampling. We
 197 choose the random partial identity matrix as the down-sampling matrix $\mathbf{\Phi}_m \in \mathbb{R}^{N' \times N}$, which is
 198 formed by the random N' columns of an N -by- N identity matrix. Thus the down-sampled
 199 signal can be expressed as

$$200 \quad \mathbf{s}'_m = \mathbf{A} \mathbf{g}_m, m = 1, 2, \dots, M, \quad (10)$$

201 where $\mathbf{A} = \mathbf{\Phi}_m \mathbf{\Psi}$. The sample rate (SR) is defined as N'/N .

202 The model in Equation 10 is an SMV model, in which the sparse vector \mathbf{g}_m can be solved by
 203 the OMP algorithm. For the linear array, each antenna element can obtain a single
 204 measurement vector. Normally, with the M times SMV model, we can get the cross-track
 205 recovery signal of one range slice. Amusing the range sampling number is N_r , the number of
 206 SMV recovery times is $M \cdot N_r$ to obtain the 3-D imaging result. Since the CS reconstruction
 207 algorithm is much more complex than the matched filtering, the SMV-based DLLA SAR
 208 imaging methods generally have high computational complexity.

In the case of the MMV model, the sparse signals of each SMV should share the same sparse structure. As shown in Figure 2, this condition cannot be satisfied if the echo signal is handled in the AT domain before the CT domain, because the CT focused results are points in each range slice, which means the sparse structures are different in different AT measurement vectors. However, as shown in Figure 3, the CT compression is before the AT compression in the proposed imaging flow process. Meanwhile, after range compression and CT compression, the focused results $\mathbf{G} = [\mathbf{g}_1, \dots, \mathbf{g}_L] \in \mathbb{C}^{N \times L}$, $1 \leq L \leq M$ are lines that are perpendicular to the AT direction in each range slice, which keeps that the multiple measurement vectors $\mathbf{S} = [\mathbf{s}_1, \dots, \mathbf{s}_L] \in \mathbb{C}^{N \times L}$ share the same sparse structure. Since the down-sampling matrix $\Phi_m \in \mathbb{R}^{N' \times N}$ is fixed, it is the same for the multiple measurement vectors $\mathbf{s}_1, \dots, \mathbf{s}_L$. That is, we can express the down-sampling matrix Φ_m as Φ for $m = 1, 2, \dots, L$. The down-sampling signal can be denoted as $\Xi = \Phi \mathbf{S}$. As a result, the $\mathbf{G} = [\mathbf{g}_1, \dots, \mathbf{g}_L]$ can be obtained by solving the following MMV model:

$$\Xi = \Phi \mathbf{S} = \Phi \Psi \mathbf{G} = \mathbf{A} \mathbf{G} \quad (11)$$

Then, the CT compression needs to solve the MMV model M/L times. The optimization problem of (11) can be described as

$$\hat{\mathbf{G}} = \min_{\mathbf{G}} F(\mathbf{G}), \quad \text{s.t.} \quad \|\Xi - \mathbf{A} \mathbf{G}\|_F^2 < \varepsilon, \quad (12)$$

where $\|\cdot\|_F$ is the Frobenius norm of a matrix, ε is an upper bound on the l_2 norm of the noise, and $F(\mathbf{G})$ is the regularization term related to the prior distribution of \mathbf{G} . To obtain better robustness, we introduced a mixed $L_{2,1}$ -norm for matrices to calculate the sparsity of \mathbf{G} . The mixed $L_{2,1}$ -norm for \mathbf{G} can be expressed as

$$\|\mathbf{G}\|_{2,1} = \left\| \begin{bmatrix} \|\mathbf{G}_1\|_2 \\ \|\mathbf{G}_2\|_2 \\ \vdots \\ \|\mathbf{G}_Q\|_2 \end{bmatrix} \right\|_1 = \sum_{i=1}^Q \sqrt{\sum_{j=1}^L |g_{ij}|^2} \quad (13)$$

where \mathbf{G}_i denote the i -th row of \mathbf{G} , $\|\cdot\|_2$ denotes the l_2 -norm for vectors, and g_{ij} is the element of \mathbf{G} at the i th row and j th column. In Equation 13, the l_2 -norms of the rows in \mathbf{G} are calculated firstly to form a column vector, and then the l_1 -norm of the formed column vector is calculated as the mixed $L_{2,1}$ -norm of \mathbf{G} . Then Equation 12 can be expressed as

$$\hat{\mathbf{G}} = \min_{\mathbf{G}} \|\mathbf{G}\|_{2,1}, \quad \text{s.t.} \quad \|\Xi - \mathbf{A} \mathbf{G}\|_F^2 < \varepsilon, \quad (14)$$

Utilizing the Lagrangian method, Equation 14 can be expressed as a regularization model

$$\hat{\mathbf{G}} = \arg \min_{\mathbf{G}} J(\mathbf{G}), \quad J(\mathbf{G}) = \|\Xi - \mathbf{A} \mathbf{G}\|_F^2 + \lambda \|\mathbf{G}\|_{2,1} \quad (15)$$

where $J(\mathbf{G})$ is the objective function and λ is the regularization parameter. According to the regularization theory [26], the regularization parameter can be $\lambda=2\beta^2$, where β is the variance of the reconstructed error. To solve Equation 15, the iterative formula of step 3) in Table 1 should be modified. As a result, we derived the gradient of the objective function $J(\mathbf{G})$ as:

$$\nabla_{\mathbf{G}} J(\mathbf{G}) = 2\mathbf{A}^H \mathbf{A} \mathbf{G} - 2\mathbf{A}^H \mathbf{\Xi} + \lambda \mathbf{\Lambda}(\mathbf{G}) \mathbf{G} \quad (16)$$

where $\mathbf{\Lambda}(\mathbf{G}) = \text{diag}(1/\|\mathbf{G}_1\|_2, 1/\|\mathbf{G}_2\|_2, \dots, 1/\|\mathbf{G}_Q\|_2)$. The k th iterative formula of \mathbf{G} can be expressed as

$$\mathbf{G}^{(k+1)} = \left(\mathbf{A}^H \mathbf{A} + \frac{\lambda}{2} \mathbf{\Lambda}(\mathbf{G}^{(k)}) \right)^{-1} \mathbf{A}^H \mathbf{\Xi} \quad (17)$$

By modifying step 3) in Table 1 as (17), the MMV-OMP algorithm based on $L_{2,1}$ norm is shown in Table 2.

Table 2: MMV-OMP algorithm based on $L_{2,1}$ norm

Input: matrix $\mathbf{\Xi}$, matrix \mathbf{A} , threshold ε ;

Initialization: residue error matrix $\mathbf{R}^{(0)} = \mathbf{\Xi}$, support set $\Omega^{(0)} = \emptyset$, sparse matrix $\mathbf{G}^{(0)} = \mathbf{0}$, iterative number $k=1$;

While $\|\mathbf{R}^{(k-1)}\|_{2,1} > \varepsilon$

Step 1: Find the new support: $\eta_k = \arg \max_{i=1,2,\dots,Q} \|\mathbf{A}_i^T \mathbf{R}^{(k-1)}\|_{2,1}$;

Step 2: Update the support set: $\Omega^{(k)} = \Omega^{(k-1)} \cup \{\eta_k\}$;

Step 3: Update the sparse matrix $\mathbf{G}^{(k)} = \left(\mathbf{A}_{\Omega^{(k)}}^H \mathbf{A}_{\Omega^{(k)}} + \frac{\lambda}{2} \mathbf{\Lambda}(\mathbf{G}^{(k-1)}) \right)^{-1} \mathbf{A}_{\Omega^{(k)}}^H \mathbf{R}^{(k-1)}$;

Step 4: Update the residue error $\mathbf{R}^{(k)} = \mathbf{\Xi} - \mathbf{A}_{\Omega^{(k)}} \mathbf{G}^{(k)}$, $k = k + 1$;

Output: sparse vector $\mathbf{G}^{(k)}$

As shown in Figure 3, the signal after CT compression can be expressed as

$$S_c(t, t_m, y_q) = \sum_{i=1}^K \text{sinc}\left(B_r \left(t - \frac{2R_0}{c}\right)\right) \zeta(y_q) \exp\left(-j \frac{2\pi}{\lambda} \frac{(vt_m - x_k)^2}{R_0}\right) \exp\left(-j \frac{4\pi}{\lambda} R_0\right) \quad (18)$$

where $\zeta(y_q)$ is the point spread function in the CT direction.

Along-track Compression

Finally, the AT compression is realized by the matched filtering in AT domain, which can be expressed as

$$S_a(t, t_m, y_q) = IFT_a \left[FT_a \left[S(t, t_m, y_q) \right] \cdot H_a \right] \\ = \sum_{k=1}^K \text{sinc} \left(T_r K_r \left(t - \frac{2R_0}{c} \right) \right) \zeta(y_q) \text{sinc} \left(B_a (vt_m - x_k) \right) \exp \left(-j \frac{4\pi}{\lambda} R_0 \right) \quad (19)$$

where FT_a and IFT_a denote the Fourier transformation and inverse Fourier transformation of AT direction, $H_a(f_a) = \exp(j\pi f_a^2 / K_a)$ is the range matched filter function, f_a is the AT frequency, K_a is the AT chirp rate, B_a is the AT bandwidth.

Results and Discussion

In this section, the simulation experiments are carried out to verify the proposed algorithm. Point targets and distributed targets are provided to evaluate the effectiveness of the proposed method. The system parameters of DLLA SAR are listed in Table 3.

Table 3: System Parameters

Center Wavelength	8 mm	Signal Bandwidth	300 MHz
Signal Pulse Width	4 us	A/D Sampling Frequency	360 MHz
Range Sampling Number	1600	Platform Flying Height	1000 m
AT Sampling Number	256	CT Sampling Number	256
AT Sampling Interval	0.01 m	CT Sampling Interval	0.01 m

Reconstruction Performance for Point Targets

At first, we discuss the relationship between the recovery probability, sampling number, and sparsity. We define the condition of one successful reconstruction is

$$\sum_{i=1}^{N_r} \sum_{m=1}^M \sum_{q=1}^Q \left| \hat{\sigma}_{imq} - \sigma_{imq} \right|^2 / \left| \sigma_{imq} \right|^2 < 0.1 \quad (20)$$

where $\hat{\sigma}_{imq}$ and σ_{imq} are the value of the imaging result and the scattering coefficient of the i th range slice, m th slow time, and the q th CT grid, respectively.

In this simulation, the range position and the AT position of the scattering points are 500m and 10m, the CT sampling number is from 10 to 128 with interval 2, L is 10, the CT positions of the scattering points are randomly generated. In the 100 Monte Carlo trials, the recovery probability is equal to the successful reconstruction times. The relation of the recovery probability and the CT sampling number is shown in Fig. 4, where (a) is for 5 scattering points and (b) is for 10 scattering points. Compared with the proposed algorithm can achieve successful reconstruction (the recovery probability is close to 1) with a lower sampling number. The reason is as follows: Suppose the recovery probability of one CT vector by Algorithm 1 is p , the recovery probability of L CT vectors by Algorithm 1 is p^L . As a result, the expected accurate recovery number of the CT vectors is $p \cdot L$. For Algorithm 2, since the L CT vectors are regarded as a whole to calculate the support set, the recovery probability of L CT vectors by Algorithm 2 is $p \cdot L / L = p \geq p^L$, which is higher than that of Algorithm 1.

Moreover, the sampling number of successful reconstructions increases with the number of scattering points, which is due to the decrease of the sparsity.

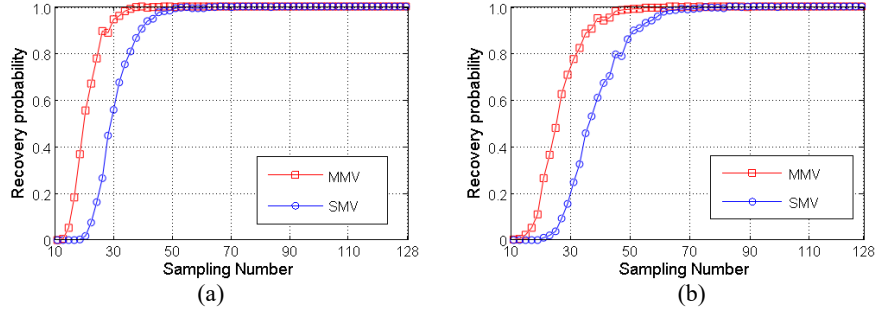


Figure 4: The relation of the recovery probability and the CT sampling number. (a) 5 scattering points, (b) 10 scattering points.

To verify the anti-noise performance, we add the white Gaussian noise into the echo signal. When SNR is -5dB and $L=128$, the imaging results of 9 random scattering points by the proposed imaging procedure are shown in Figure 5. Figure 5a and Figure 5b are the results after MMV-based CT compression and SMV-based CT compression, respectively. On the basis of Figure 5a and Figure 5b, Figure 5c and Figure 5d accomplished the AT compression, respectively. The reconstructed scattering points are marked with a blue circle in Figure 5c and Figure 5d. It is clear that the signal is almost involved by the noise in Figure 5b so that 3 scattering points are lost in Figure 5d. However, all scattering points have been successfully reconstructed in Figure 5c. That is, the MMV model can enhance the anti-noise ability.

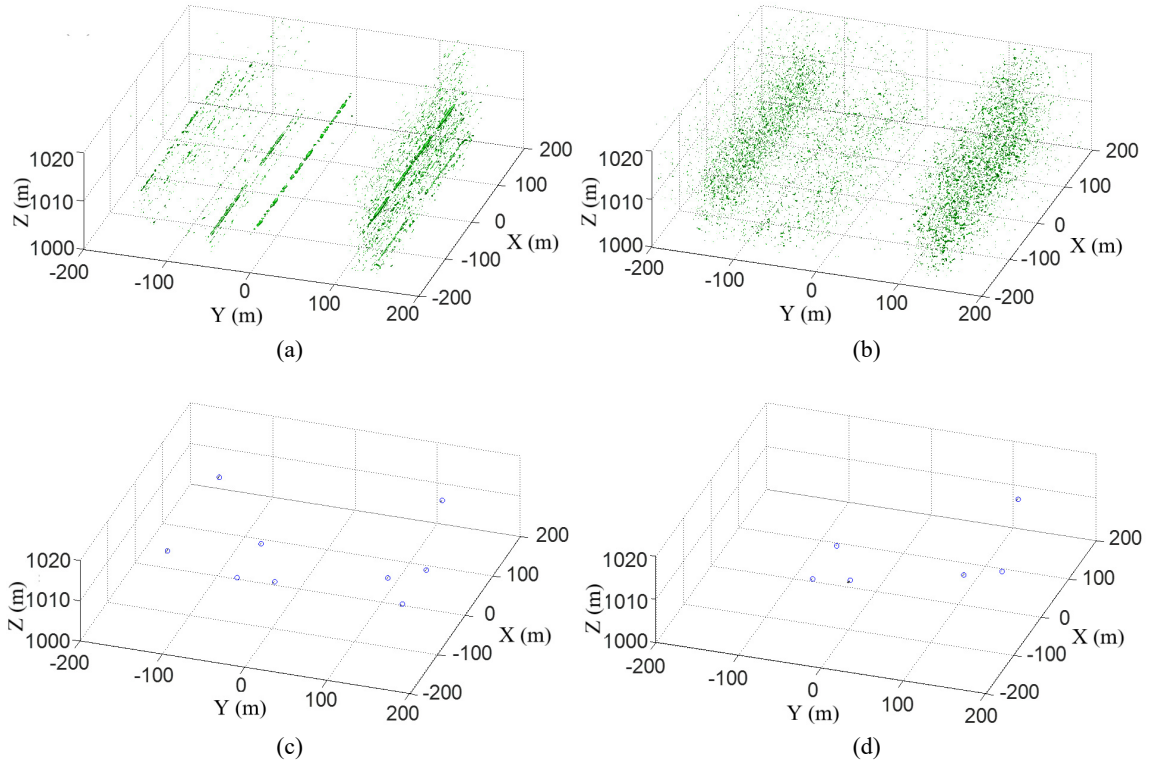


Figure 5: The imaging results of 9 random scattering points when SNR is -5dB and $L=128$. (a) Completed the range compression and MMV-based CT reconstruction, (b) completed the range compression and SMV-based CT reconstruction, (c) AT compression result of (a), (d) AT compression result of (b).

Then we discuss the relation between the recovery probability and the multi-measurement number L . We calculate the recovery probability when $L=1, 4, 16, 64, 128$. The scope of SNR is $-15\text{ dB}\sim 1\text{ dB}$ with 1 dB step. The relation of the recovery probability, SNR, and the multi-measurement number is shown in Fig. 6. It can be seen that under the same SNR, the smaller the multi-measurement number L is, the lower the recovery probability is.

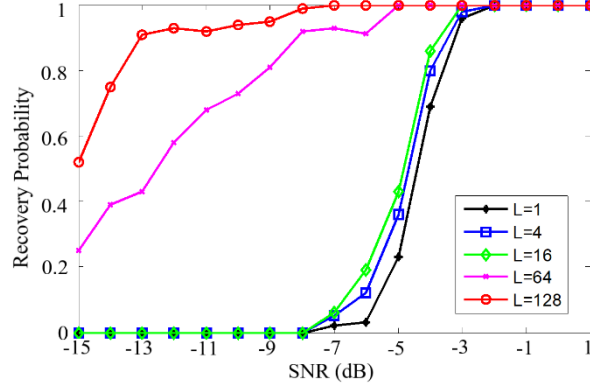
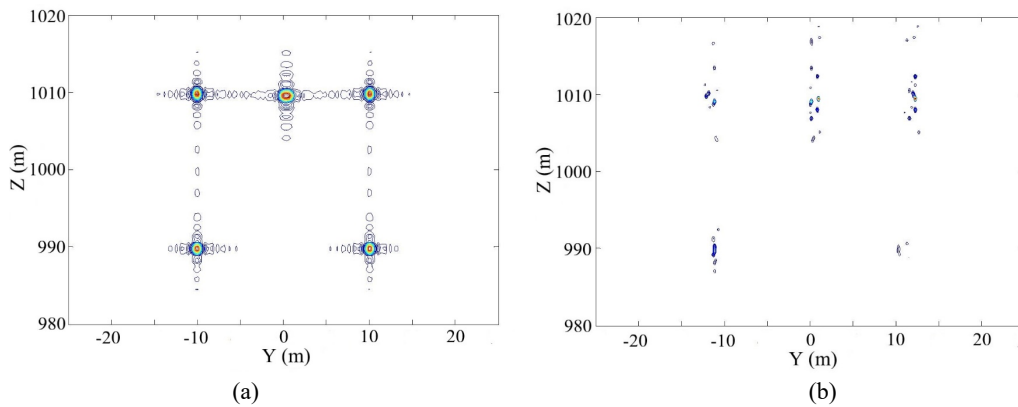


Figure 6: The relation of the recovery probability, SNR, and the multi-measurement number.

To verify the super-resolution performance of the proposed method, we set 6 scattering points in the same AT cell. Since the Rayleigh resolution in the CT direction is about 1.5m according to the system parameters, the CT distance between the two points in the middle is 1m , which is less than the CT Rayleigh resolution. As a result, the CT super-resolution is achieved if the two points in the middle can be separated. The imaging results of the 6 scattering points on the range-CT plane are shown in Figure 7. Figure 7a is obtained by the 3DRD method, in which the CT compression is realized by matched filtering so that the middle two points are overlapped. Figure 7b and Figure 7c are obtained by the SMV-based imaging method when SNR is -5dB and 0dB , respectively. Although the two points in the middle can be separated in Figure 7c, the scattering points are unfocused in Figure 7b. As a result, the robustness of the l_1 -norm-based models is unsatisfactory. Figure 7d is obtained by the proposed MMV-based imaging method when SNR is -5dB and $L=128$. It can be seen that the scattering points are focused. Moreover, the two points in the middle are separated clearly, which means the proposed method can achieve the CT super-resolution in the lower SNR environment.



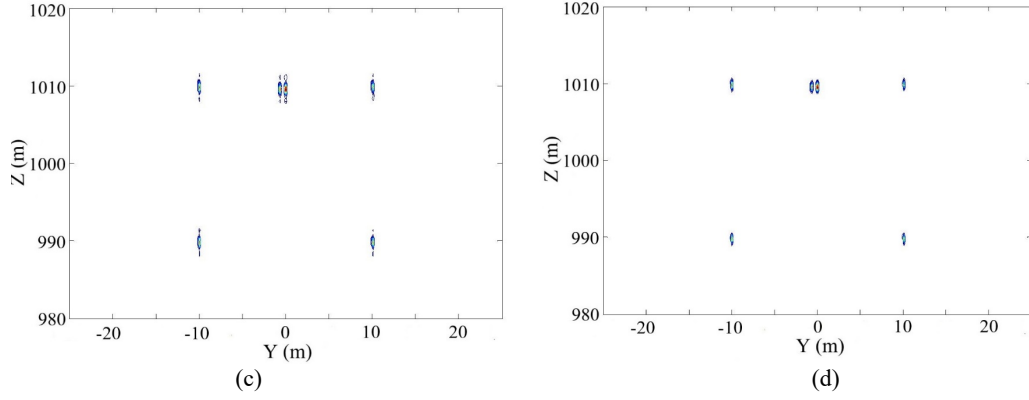


Figure 7: The imaging results of the 6 scattering points on the range-CT plane. (a) 3-D RD method when SNR is -5dB, (b) SMV-based method when SNR is 0dB, (c) SMV-based method when SNR is -5dB, (d) the proposed MMV-based method when SNR is -5dB and $L=128$.

To compare the computational complexity of the methods, we recall the SMV-OMP algorithm and the MMV-OMP algorithm, in which the main computational burden includes the internal product calculation in step 1) and the matrix inversion in step 3). The comparison of computational complexity is shown in Table 2. Because the range sampling number and the AT sampling number are N_r and M , the number of the CT vectors to be reconstructed is $M \cdot N_r$. To obtain the imaging results, Algorithm 1 needs to run $M \cdot N_r$ times. As a result, step 1) needs to calculate the internal product $O(KN_rMN)$ times, and step 3) needs to calculate the matrix inversion $O(KN_rM)$ times. Since Algorithm 2 can deal L CT vectors once, it needs to run N_rM/L times to obtain the imaging result. As a result, step 1) also needs to calculate the internal product $O(KN_rMN)$ times, but step 3) only needs to calculate the matrix inversion $O(KN_rM/L)$ times, where $1 \leq L \leq M$. The sparse level K is positively related to the time cost. The multi-measured vector number L has an important influence on the time cost.

Table 4 Analysis of complexity

	SMV-based method	Proposed MMV-based method
Times of internal product	$O(KN_rMN)$	$O(KN_rM)$
Times of matrix inversion	$O(KN_rMN)$	$O(KN_rM/L)$

Experiment for distributed extended targets

To validate the proposed method further, we use a SAR image and the corresponding DEM data to generate the echo of the distributed targets. As shown in Figure. 6, the simulated DLLA SAR data generation needs the position of scatters and the coefficient of scatters, which are from the DEM data and the SAR image for a same region, respectively. This data generation mode for DLLA 3-D SAR has been widely used to verify the imaging performance of distributed extended targets [16-20]. At first, the scatters distribute uniformly in the azimuth direction and cross-track direction with 1 m interval, which is less than the azimuth and cross-track Rayleigh resolution 1.5 m. The scatter number in the simulation is $N_p N_q = 400 \times 400$. The white Gaussian noise is added to the signal before imaging and the SNR is -5 dB.

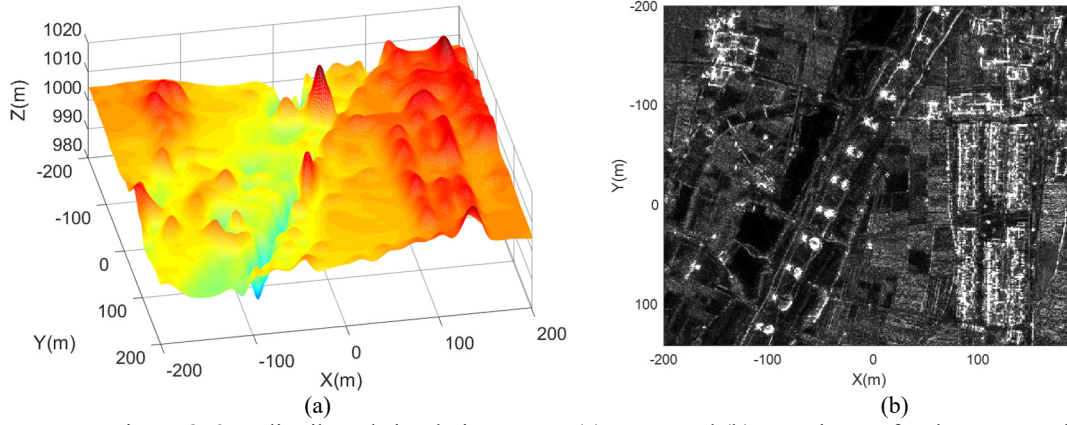


Figure 8: 3-D distributed simulation scene. (a) DEM and (b) SAR image for the same region.

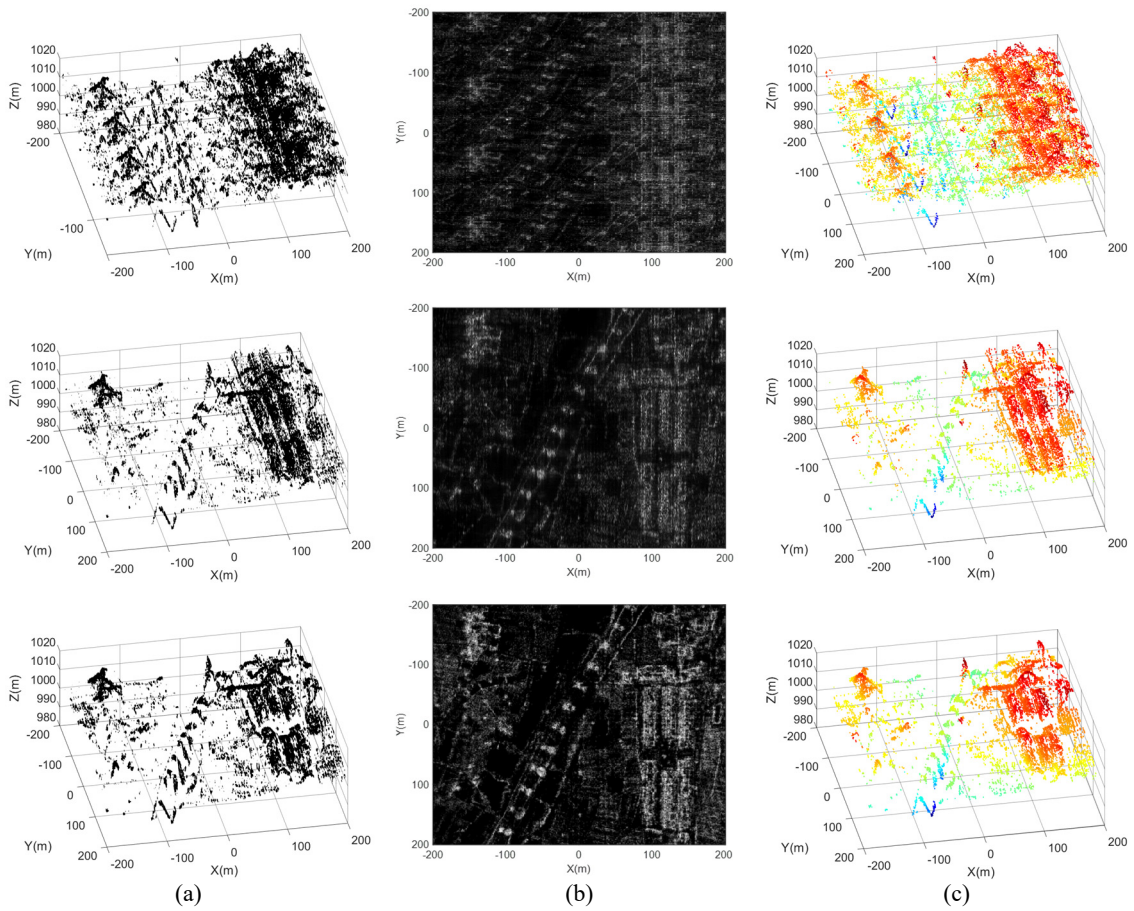


Figure 9: Imaging results of the 3-D distributed scene by 3DRD, SMV-OMP, and the proposed method from top to bottom when the SNR is -5dB and the sampling rate is 25%. (a) 3-D reconstructed images. (b) X-Y plane projection images. (c) 3-D reconstructed point cloud coloured by height.

As shown in Figure 9, when the SNR is -5dB and the sampling rate is 25%, the imaging results of the 3-D distributed scene by 3DRD, SMV-OMP, and the proposed method are listed from top to bottom, respectively. Figure 9(a), (b), and (c) show the 3-D reconstructed images, the corresponding X-Y plane projection images, and the 3-D reconstructed point cloud coloured by height. In the first row of Figure 9, the CT compression in 3DRD is realized by matched filtering, and the CT ambiguity appears when the sampling rate is 25%. It means that the 3DRD method has no ability to deal with sparse data. In the second row of Figure 9, the CT compression is realized by SMV-OMP, and some scatters are out of focus

when the SNR is -5dB. It means that the robustness of the imaging method based on SMV-OMP is unsatisfactory in the low Signal-to-Noise Rate (SNR) environment. In the third row of Figure 9, the CT compression is realized by the proposed MMV-OMP when $L=128$, and the imaging results focus much better than those of the SMV-OMP. It means that the proposed method can obtain better performance in the low SNR environment.

Table 5 Imaging performance of the distributed targets

	3DRD	SMV-OMP	proposed method
Relative Mean Square Error	0.8734	0.1905	0.0847
Mean running time (s)	6.85s	154.72s	33.24s

To quantify the imaging results accuracy, the Relative Mean Square Error (RMSE) of the 3-D imaging results is defined as $\frac{1}{N_p N_q} \sum_{k=1}^{N_p N_q} |\hat{\sigma}_k - \sigma_k|^2 / |\sigma_k|^2$, where $N_p N_q$ is the scatter number, $\hat{\sigma}_k$ is the reconstructed value of the k th scatter, σ_k is the true value according to Figure 8(b). The RMSE of the 3-D imaging results in figure 9(a) is shown in Table 5. The proposed method has a smaller RMSE. Moreover, the total running time is also shown in Table 5. The proposed method has a shorter running time than the imaging method based on SMV-OMP, which can indicate the advantages of the proposed method.

Conclusions

In this paper, we propose a novel imaging method for DLLA 3D SAR based on the MMV model with $L_{2,1}$ norm. Specifically, the imaging problem can be transformed into a sparse regularization model based on the MMV model since we construct the same CT sparse structure of different pulses by exchanging the processing sequence of the CT compression and the AT compression. Moreover, the mixed $L_{2,1}$ -norm is introduced into the regularization term of the MMV model and the corresponding MMV-OMP algorithm is designed. The proposed method can obtain the CT super-resolution in the lower SNR environment and require lower computation compared with the conventional methods, which is verified by the simulation experiments of point targets and distributed targets.

Conflicts of Interest

The authors declare that there are no conflicts of interest regarding the publication of this paper.

Funding Statement

This work was supported in part by the National Natural Science Foundation of China under Grant 61631019 and 61971434, and the Natural Science Foundation of Shanxi Province under Grant 2020JQ-480.

Acknowledgments

The authors would like to thank the Institute of Electrics, Chinese Academy of Sciences for sharing the experimental data in this paper. The author Le Kang and the author Tian-chi Sun contributed equally to this work.

413 References

- 414 [1] X. X. Zhu, S. Montazeri, M. Ali, et al, "Deep Learning Meets SAR: Concepts, Models, Pitfalls, and
415 Perspectives," *IEEE Geoscience and Remote Sensing Magazine*, doi: 10.1109/MGRS.2020.3046356.
- 416 [2] M. Soumekh, *Synthetic Aperture Radar Signal Processing with Matlab Algorithms*, Wiley, New York,
417 NY, USA, 1999.
- 418 [3] E. Aguilera, M. Nannini, A. Reigber, "Wavelet-based compressed sensing for SAR tomography of
419 forested areas," *IEEE Transactions on Geoscience and Remote Sensing*, vol. 51, no. 12, pp. 5283–
420 5295, 2013.
- 421 [4] Y. Lin, W. Hong, W. X. Tan, Y. P. Wang, "Airborne circular SAR imaging: results at P-band," in
422 *Proceedings of the IEEE International Geoscience and Remote Sensing Symposium (IGARSS '12)*, pp.
423 5594–5597, Munich, July 2012,
- 424 [5] C. H. Gierull, "On a concept for an airborne downward-looking imaging radar," *AEU-International
425 Journal of Electronics and Communications*, vol. 53, no. 6, pp. 295–304, 1999.
- 426 [6] R. Giret, H. Jeuland, and P. Enert, "A study of a 3D-SAR concept for a millimeter-wave imaging radar
427 onboard an UAV," in *Proceedings of the European Radar Conference*, pp. 201–204, Amsterdam, The
428 Netherlands, 2004,
- 429 [7] J. Klare, D. Cerutti-Maori, A. Brenner, et al, "Image quality analysis of the vibrating sparse MIMO
430 antenna array of the airborne 3D imaging radar ARTINO," in *Proceedings of the IEEE International
431 Geoscience and Remote Sensing Symposium (IGARSS '07)*, pp. 5310–5314, Barcelona, Spain, July
432 2007.
- 433 [8] J. F. Nouvel, H. Jeuland, G. Bonin, S. Roques, O. Du Plessis, and J. Peyret, "A Ka band imaging radar:
434 DRIVE on board ONERA motorglider," in *Proceedings of the IEEE International Geoscience and
435 Remote Sensing Symposium (IGARSS '06)*, pp. 134–136, Denver, Colo, USA, August 2006.
- 436 [9] L. Du, Y. P. Wang, and W. Hong, "A three-dimensional range migration algorithm for downward-
437 looking 3-D SAR with single-transmitting and multiple-receiving linear array antennas," *EURASIP
438 Journal on Advances in Signal Processing*, vol. 2010, Article ID 957916, 15 pages, 2010.
- 439 [10] D. H. Zhang and X. L. Zhang, "Downward-looking 3-D linear array SAR imaging based on chirp
440 scaling algorithm," in *Proceedings of the 2nd Asian-Pacific Conference on Synthetic Aperture Radar
441 (APSAR '09)*, pp. 1043–1046, Xi'an China, October 2009.
- 442 [11] X. M. Peng, W. Hong, and Y. P. Wang, "Polar format imaging algorithm with wave-front curvature
443 phase error compensation for airborne DLSLA three-dimensional SAR," *IEEE Geoscience and Remote
444 Sensing Letters*, vol. 11, no. 6, pp. 1036–1040, 2014.
- 445 [12] D. L. Donoho, "Compressed sensing," *IEEE Transactions on Information Theory*, 52, (4), pp. 1289–
446 1306, 2006.
- 447 [13] E. J. Candes, J. Romberg, and T. Tao, "Robust uncertainty principles: exact signal reconstruction from
448 highly incomplete frequency information," *IEEE Transactions on Information Theory*, vol. 52, no. 2,
449 pp. 489–509, 2006.
- 450 [14] X. Ren, L. Chen, and J. Yang, "3-D imaging algorithm for down-looking MIMO array SAR based on
451 bayesian compressive sensing," *International Journal of Antennas & Propagation*, vol. 2014, Article
452 ID 612326, 2014.
- 453 [15] S. Q. Zhang, Y. T. Zhu, G. G. Dong, and G. Y. Kuang, "Truncated SVD based compressive sensing for
454 downward-looking three-dimensional SAR imaging with uniform/nonuniform linear array," *IEEE
455 Geoscience and Remote Sensing Letters*, vol. 12, no. 9, pp. 1853–1857, 2015.
- 456 [16] X. M. Peng, W. X. Tan, W. Hong, et al, "Airborne DLSLA 3-D SAR Image Reconstruction by
457 Combination of Polar Formatting and L1 Regularization," *IEEE Transactions on Geoscience and
458 Remote Sensing*, vol. 54, no. 1, pp. 213–226, 2016.
- 459 [17] Q. Bao, K. Y. Han, L. Yun, B. C. Zhang, J. G. Liu, and W. Hong, "Imaging method for downward-
460 looking sparse linear array three-dimensional synthetic aperture radar based on reweighted atomic
461 norm," *Journal of Applied Remote Sensing*, vol. 10, no. 1, Article ID 015008, 13 pages, 2016.
- 462 [18] Q. Bao, K. Y. Han, X. M. Peng, W. Hong, B. C. Zhang, and W. X. Tan, "DLSLA 3-D SAR imaging
463 algorithm for off-grid targets based on pseudo-polar formatting and atomic norm minimization,"
464 *Science China Information Sciences*, vol. 59, no. 6, Article ID 062310, 2016. doi: 10.1007/s11432-015-
465 5477-5.
- 466 [19] Q. Bao, X. M. Peng, Z. R. Wang, L. Yun, and W. Hong, "DLSLA 3-D SAR Imaging Based on
467 Reweighted Gridless Sparse Recovery Method," *IEEE Geoscience and Remote Sensing Letters*, vol.
468 13, no. 6, pp. 841–845, 2016.

- [20] Q. Bao, C. L. Jiang, L. Yun, W. X. Tan, Z. R. Wang, and W. Hong, "Measurement matrix optimization and mismatch problem compensation for DLSLA 3-D SAR cross-track reconstruction" *Sensors*, vol. 16, no. 8, pp. 1333-1349, 2016.
- [21] J. Chen, X. Huo, "Theoretical results on sparse representations of multiple-measurement vectors," *IEEE Transactions on Signal Processing*, vol. 54, no. 12, pp. 4634-4643, 2006.
- [22] Y. Chen, Q. Zhang, Y. A. Chen, and L. Sun, "Modified multiple measurement vectors model for squinted synthetic aperture radar imaging," *Journal of Electronic Imaging*, vol.26 no.3, 2017.
- [23] D. Y. Ao, R. Wang, C. Hu, and Y. H. Li, "A sparse sar imaging method based on multiple measurement vectors model," *Remote Sensing*, vol. 9, no. 3, 297, 2017. doi:10.3390/rs9030297.
- [24] Q. Y. Liu, Q. Zhang, F. F. Gu, "Downward-Looking Linear Array 3D SAR Imaging Based on Multiple Measurement Vectors Model and Continuous Compressive Sensing". *Journal of Sensors*, vol. 2017, Article ID 6207828, 11 pages, 2017.
- [25] S. Yi, L. Song, "Sparse Signals Recovery from Noisy Measurements by Orthogonal Matching Pursuit". *Inverse Problems & Imaging*, vol. 9, no. 1, pp.231-238, 2015.
- [26] Tikhonov, N.: 'Regularization of incorrectly posed problems', *Soviet Mathematics Doklady*, vol.4, no.1, pp.1624-1627, 1963.